RSC Advances

PAPER

View Article Online
View Journal | View Issue

Cite this: *RSC Adv.*, 2016, **6**, 31514

Supported polymer magnets with high catalytic performance in the green reduction of nitroaromatic compounds

J. Safari,* S. Gandomi-Ravandi and Z. Haghighi

Received 16th December 2015
Accepted 11th March 2016

DOI: 10.1039/c5ra26613k

www.rsc.org/advances

Magnetic Fe_3O_4 nanoparticles (MNPs) were prepared by a simple co-precipitation method using molar ratios of $Fe^{2+}:Fe^{3+} = 1:2$ in ammonia solution, and subsequently were modified with tetraethyl orthosilicate (TEOS) *via* a modified Stöber method and also with 3-aminopropyl triethylenesilane (APTES) *via* a silanization reaction. Then, a layer of TiO_2 shell was coated directly onto the silica coated magnetite core–shell nanoparticles (Fe_3O_4@SiO_2) followed by dispersion of a Ag nanoparticle layer on the surface of the TiO_2 shell. Also, the amino-silane coated magnetite nanoparticles (Fe_3O_4-APTES) were successfully coated with polyethylene glycol (PEG) *via* the formation of covalent bonds between $-NH_2$ and $-COOH$ to afford well-defined polymer-coated magnetic nanoparticles. Several transition metal nanoparticles (such as Cu, Ag, Co, Ni, Pb, Zn and Mn) were then loaded on the surface of Fe_3O_4-APTES–PEG. We exhibit herein the synthesis and modification of magnetic nanoparticles as solid phase catalysts and their use in the reduction of nitroaromatics (nitrophenols, nitroanilines) in the presence of an excess amount of sodium borohydride ($NaBH_4$). The kinetic activity of the catalysts used in the reduction of nitroaromatic compounds was studied using UV-visible spectrophotometer. The reduction reaction followed first-order kinetics. Moreover, these magnetic core–shell nanocomposites showed convenient magnetic separability as well as quite good stability after five recycles.

1. Introduction

Magnetite, the most useful paramagnetic material, has an inverse spinel cubic structure in which the oxygen atom forms closed packing and the iron cations take up the interstitial tetrahedral or octahedral positions.[1] Magnetic nanoparticles (MNPs), especially Fe_3O_4, have received considerable attention due to their interesting properties including high biocompatibility, strong superparamagnetism, low toxicity, feasibility of preparation and easy separation under external magnetic fields.[2,3] Magnetic nanoparticles have shown many applications in various fields, particularly in biomedicine and bioengineering, such as high-density information storage,[4,5] biolabeling,[6] DNA detection,[7] immunoassay,[8] tumor therapy,[9] bioelectrochemistry,[10] enzyme-immobilization,[11,12] biosensors,[13] targeted drug delivery labeling,[14,15] magnetic resonance imaging (MRI) contrast enhancement,[16,17] magnetic hyperthermia treatment of cancers,[18,19] as well as bio separation in life-science.[20,21] Oxidation, acid erosion and aggregation of Fe_3O_4 nanoparticles limit their extensive applications due to strong dipole–dipole attraction between particles.[22] Therefore, a protection layer is required to improve its chemical stability, dispersibility, oxidation resistance and the ability to functionalize.[23] The surface modification of magnetic nanoparticles has been developed by biocompatible organic species[24] (surfactants and polymers) or inorganic layers[25] (silica, carbon and metals). It has been reported that silica as an inorganic protective shell is appropriate option to coat the Fe_3O_4 nanoparticles to form Fe_3O_4@SiO_2 core–shell structures. It is worth noting that silica coating layer yields a protective, non-toxic, inert, biocompatible, and hydrophilic surface with excellent anchoring points for appropriate surface modification.[26,27] Meanwhile, the outer silica shells can inhibit the aggregation of the Fe_3O_4 NPs in liquid and can improve the chemical stability.[28] Moreover, the existence of abundant silanol (Si/OH) groups on the silica layer provides covalent attachment of a variety of specific groups.[29] Typically, two of the most common approaches for coating silica on magnetic nanoparticles are the alkaline hydrolysis of tetraethyl orthosilicate (TEOS) in the ethanol–ammonia mixture[30] (namely the well-known Stöber process),[31] and the microemulsion system in which inverse micelles or "droplets" were applied to confine and control the coating of silica on magnetic nanoparticle cores.[32]

Many studies on the photocatalytic influence of core–shell structures based on photoactive titania shell (TiO_2), silica layer, and magnetic core have been reported.[33,34] Combining TiO_2 photocatalysts with magnetic nanoparticles will provide high photocatalytic activity and will improve separation capability.[35]

Laboratory of Organic Compound Research, Department of Organic Chemistry, College of Chemistry, University of Kashan, P.O. Box 87317-51167, Kashan, I. R. Iran. E-mail: safari@kashanu.ac.ir; Fax: +98-31-5591-2397; Tel: +98-31-5591-2320

The presence of a SiO_2 layer as a hole–electron trap center between magnetic core and TiO_2 shell improves the photocatalytic activity of the nanomaterial.[36] Metallic nanoshells composed of a magnetic core and a noble metal shell have been extensively investigated in heterogeneous catalytic processes.[37] The incorporation of magnetic nanoparticles into Ag NPs is most favoured due to their unique catalytic, conductive and optical properties.[38] Unfortunately, these nanoshells are generally unstable owing to aggregation of the metal nanoparticles. Therefore, silica has been reported as suitable supporting matrix to immobilize Ag nanoparticles.[39] It has been reported that the surface of magnetic NPs (MNPs) can also be functionalized with the organosilanes agent of 3-aminopropyl triethoxysilane $(NH_2(CH_2)_3Si(OC_2H_5)_3)$ (APTES).[40] Organosilanes are non-poisonous and bifunctional molecules which they can be easily attached to the hydroxyl groups of inorganic surfaces *via* formation of covalent and strong Si–O–M bonds (M = the metal from inorganic substrate).[41] Such surface modification improves the biocompatibility and makes basic surface (*via* high density of surface functional group of $-NH_2$ on the silica layer) to immobilize other metals, polymers or other substances.[42] Among various types of materials, poly(ethylene glycol) (PEG) is of current research interest to form well-dispersed surface functionalized biocompatible magnetic nanoparticles (MNPs). PEG, a biologically acceptable polymer containing of ethylene oxide as repeating units, was used extensively to stabilize magnetic nanoparticles because of its unique properties such as biocompatibility, hydrophilicity, non-toxicity, flexibility, and non-immunogenicity.[43] In recent years, it is well-established that the polymer matrices are excellent host materials for metal nanoparticles to fabricate composite materials consisting of polymer matrix encapsulated metal particles.[44]

p-Nitrophenol (PNP) is one of the most important organic and priority pollutants in industrial and agricultural wastewater. It is a common by-product from the production of synthetic dyes, the hydrolysis of the organophosphate pesticides, insecticides, and herbicides,[45] which is stable in the environment and resists biodegradation.[46] While *p*-aminophenol (PAP) is a potential intermediate in the preparation of many analgesic and antipyretic drugs such as paracetamol, acetanilide and phenacetin and is widely used as a corrosion inhibitor in paints, hair-dyeing agent, photographic developer in fuels, and anti-corrosion lubricant inhibitor in fuels.[47] Due to the significance of aminophenols, it is highly desirable to develop a green and effective catalyst for direct catalytic reduction of *p*-nitrophenol.[48] The catalytic reduction of 4-nitrophenol (4-NP) over magnetite nanoparticles (MNPs) in the presence of $NaBH_4$ as the hydride source has been extensively investigated to efficiently produce 4-aminophenol (4-AP).[49] Additional, conducting polymer–metal nanocomposites have been widely used in catalysis. Indeed, the polymer matrix affords flexible functionalities to control host–guest interaction and metal nanoparticles owing to high Fermi potential lead to lowering of reduction potential for catalyzing electron-transfer reactions.[50]

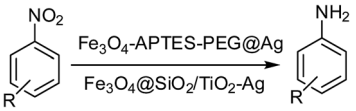

Scheme 1 The catalytic reduction of nitroaromatics to aminoaromatics by $NaBH_4$ over Fe_3O_4@APTES/PEG/Ag and Fe_3O_4@SiO_2/TiO_2/Ag core–shell nanostructures.

In the present study, a facile, low-cost and economically useful synthetic route was developed to prepare magnetite-based core–shell nanocomposites. Subsequently, the catalytic activity of the composites on 4-nitroaromatics reduction was investigated in the presence of $NaBH_4$ with UV light irradiation. Furthermore, its reusability and the corresponding kinetic properties were also evaluated. Scheme 1 depicts the catalytic performance of Fe_3O_4@SiO_2/TiO_2/Ag and Fe_3O_4@APTES/PEG/Ag core–shell structures in the reduction of nitrophenols to aminophenols by $NaBH_4$. The present synthetic procedures are very easy, cost effective, straightforward and green.

2. Results and discussion

2.1. Characterization of core–shell structure magnetic particles

X-ray powder diffraction was used to determine the crystallography, phase structure, purity and crystallite size of the sample. Fig. 1 presents XRD patterns of pure Fe_3O_4 and the corresponding magnetic core–shell nanocomposites. Six diffraction peaks occurred at 2θ of 30.1, 35.5, 43.1, 53.4, 57, and 62.7 can be indexed as (220), (311), (422), (400), (511), and (440) Bragg reflection revealing the cubic spinel structure of Fe_3O_4 in agreement with standard magnetite XRD patterns. Moreover, the characteristic peaks are strong and sharp, indicating good crystallization of the as-prepared magnetite NPs. The average crystal size of the MNPs cores was calculated to be 12 nm using the full width at half-maximum of the peak at $2\theta = 35.5^\circ$ in the Debye–Scherrer equation. In curve (b) of Fig. 1A, it can be seen that the diffraction peaks of Fe_3O_4@SiO_2 are similar to those of the parent Fe_3O_4 with slight intensity changes without crystal phase change because of the effect of the amorphous silica shell. Furthermore, the XRD pattern also reveals a broad band of amorphous SiO_2 at $2\theta = 23.5^\circ$ in addition to the characteristic peaks of Fe_3O_4. In Fig. 1A (curve c) in addition to the diffraction peaks ascribed to the magnetite component and amorphous silica, the obvious diffraction peaks located at 26°, 38°, 48°, 55°, 57°, and 62° attributed to (101), (004), (200), (105), (211), and (204) planes of the anatase phase of TiO_2 well. The intensity of Fe_3O_4 peaks reduces compared with pure Fe_3O_4 in Fig. 1A (curve a). Curve (d) of Fig. 1A shows the patterns of Fe_3O_4@SiO_2@TiO_2/Ag particles, in which the peaks (at $2\theta = 38$, 44, 64, and 77) were revealed corresponding to (111), (220), (311), (400) for pure silver as the shell. The results confirmed that Ag NPs were successfully coated on the surface of Fe_3O_4@SiO_2@TiO_2. Fig. 1B (curve b) shows the results of XRD analysis for Fe_3O_4@APTES nanoparticles. A weak broad band (27°) appeared in XRD pattern of the APTES-MNPs which could be devoted to the

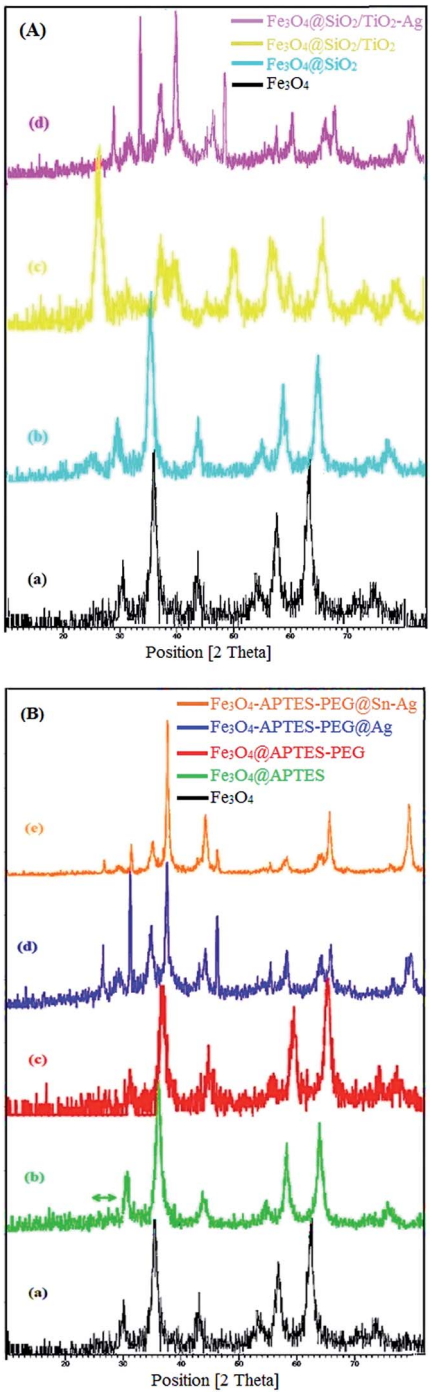

Fig. 1 X-ray powder diffraction (XRD) patterns in curve (A) for (a) Fe_3O_4 MNPs (b) Fe_3O_4@SiO_2 MNPs, (c) Fe_3O_4@SiO_2/TiO_2, (d) Fe_3O_4@SiO_2/TiO_2–Ag and in curve (B) for (a) Fe_3O_4 MNPs (b) Fe_3O_4@APTES (c) Fe_3O_4@APTES–PEG (d) Fe_3O_4-APTES–PEG@Ag, (e) Fe_3O_4-APTES–PEG@Sn–Ag.

amorphous silane shell formed surrounding the magnetic cores. The same characteristic peaks also has been presented in Fig. 1B (curve c) in which only the peaks intensity and width changed after coating with amino-silane and PEG, showing the crystalline structure of the modified magnetite was retained. In curves (d and e) of Fig. 1B, the presence of silver (Ag) is confirmed with the characteristic diffraction peaks at about 38, 44, 65 and 78, which intensity of peaks are (170, 110, 124, 102) and (450, 178, 190, 200) for Fe_3O_4-APTES–PEG@Ag prepared by $NaBH_4$ and $SnCl_2$, respectively.

The surface morphology, agglomeration state of the particles and the particle size distribution of the products were investigated by scanning electronic microscopy (SEM) as shown in Fig. 2a–i. Fig. 2a shows that the bare Fe_3O_4 particles with

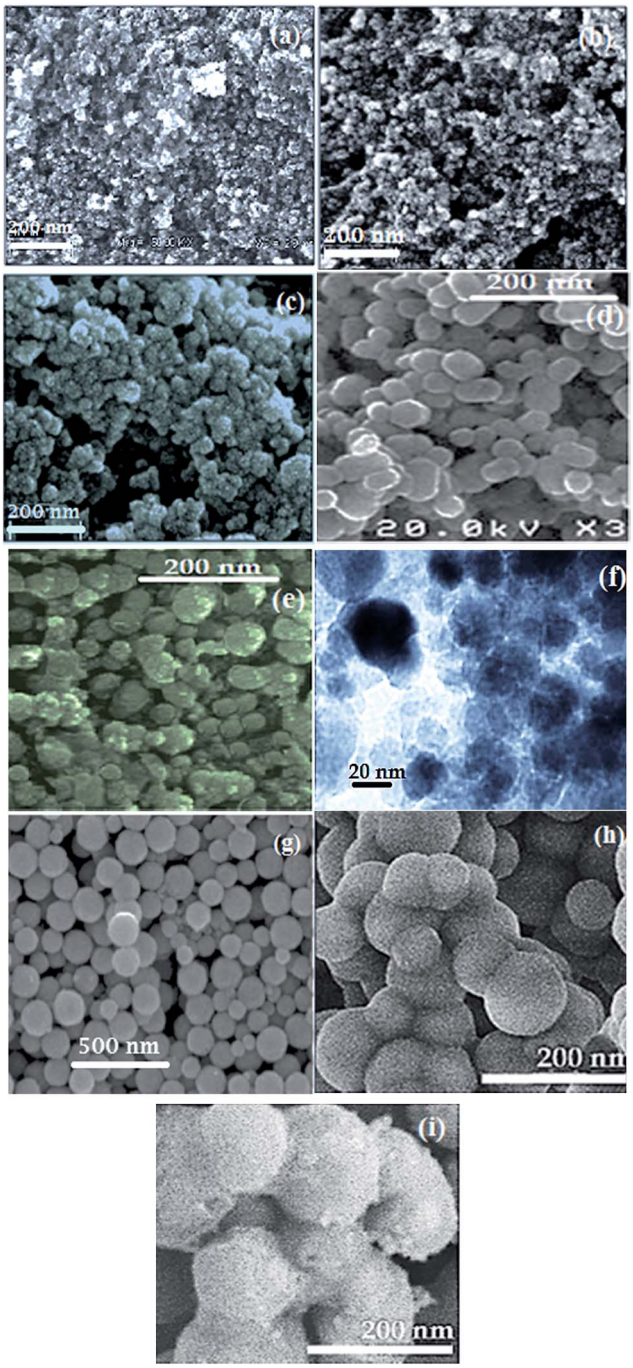

Fig. 2 SEM and TEM micrographs of (a) Fe_3O_4 MNPs, (b) Fe_3O_4-APTES MNPs, (c) Fe_3O_4@APTES–PEG, (d) Fe_3O_4-APTES–PEG@Ag, (e) Fe_3O_4-APTES–PEG@Sn–Ag, (f) Fe_3O_4-APTES–PEG@Ag, (g) Fe_3O_4@SiO_2 MNPs, (h) Fe_3O_4@SiO_2/TiO_2, (i) Fe_3O_4@SiO_2/TiO_2–Ag MNPs.

uniform morphology have a rough surface and particles size of about 18 nm. The SEM image of the APTES-modified Fe_3O_4 (Fe_3O_4@APTES) MNPs shows that the average size of these particles is about 27 nm and in comparison with the original magnetite particles, there are no obvious change in morphology and dispersibility (Fig. 2b). The SEM image in Fig. 2c has clearly shown that Fe_3O_4@APTES–PEG with uniform structure has nearly spherical shape with particle size of 40 nm. Indeed, Fe_3O_4@APTES–PEG nanoparticles still retain the same morphological properties of magnetite except for a larger particle size and smoother surface owing to the surface coated with polymer shells. SEM images (Fig. 2d and e) of Ag coated on Fe_3O_4-APTES–PEG using $NaBH_4$ and $SnCl_2$ indicate an approximate spherical shape with uniform dispersion and the average size of around 50 and 55 nm, respectively. To further investigate the Fe_3O_4-APTES–PEG@Ag the representative TEM image was used as shown in Fig. 2f. As can be seen in TEM image, the core–shell structure of the synthesized samples shows a dark areas with the particle size of about 10 nm. All of these nanoparticles have spherical shape with homogeneous dispersion. From Fig. 2g, it can be seen that the SiO_2-coated Fe_3O_4 nanoparticles displayed well-dispersed spherical shapes with a smooth surface and the average particle size of 50 nm. As shown in the Fig. 2h, it is clear that the particle size of the $Fe_3O_4/SiO_2/TiO_2$ core–shell increases (82 nm) compared with the precursor, and the dispersion of these spherical nanoparticles is nearly uniform. According to the SEM image of Fig. 2i, the morphology and surface of silver coated $Fe_3O_4/SiO_2/TiO_2$ unchanged but the size of the microsphere was larger (90 nm).

The successful surface modification of the MNPs was confirmed by FT-IR spectra. The resulting spectra have been represented in Fig. 3A and B. According to curve of (a) in Fig. 3A, the characteristic absorption peaks at 441 and 579 cm^{-1} are attributed to the Fe–O vibration from the magnetite phase. The broad absorption bands centered around 3430 and 1629 cm^{-1} are related to the H–O–H stretching modes and bending vibration of the free or physically adsorbed water, respectively. The presence of silica coating could also be confirmed by FTIR spectrum (Fig. 3A, curve of (b)). The broad high-intensity band at 1034 cm^{-1} is attributed to the asymmetric stretching vibration of Si–O–Si bonds, while the characteristic bands at 457 and 591 cm^{-1} correspond to the Si–O–Si or O–Si–O bending modes and Si–O–Fe stretching vibrations. The absorption peaks at 1633 and 3433 cm^{-1} are assigned to bending and stretching vibration modes of –OH, respectively. In the spectrum of Fe_3O_4-APTES, the absorption bond at 1019 cm^{-1} can be referred to the stretching vibration of the Si–O–Si bond whereas the anti-symmetric and symmetric saturated C–H stretching vibrations appeared at 2929 cm^{-1} and 2857 cm^{-1}, respectively. The two bands at 1627 cm^{-1} and 3434 cm^{-1} are ascribed to the NH_2 bending mode of free NH_2 group and N–H stretching vibration overlapped by the O–H stretching vibration, respectively. In the meantime, the Fe–O–Si bonds cannot be seen at around 585 cm^{-1} due to overlapped Fe–O stretching vibration of magnetic NPs. Moreover, the absorption at 2924 cm^{-1} (–CH_2 stretching), 1719 and 1610 cm^{-1} (C═N stretching) and 1102 cm^{-1} (–C–O–C– stretching) indicated the existence of PEG in the composite

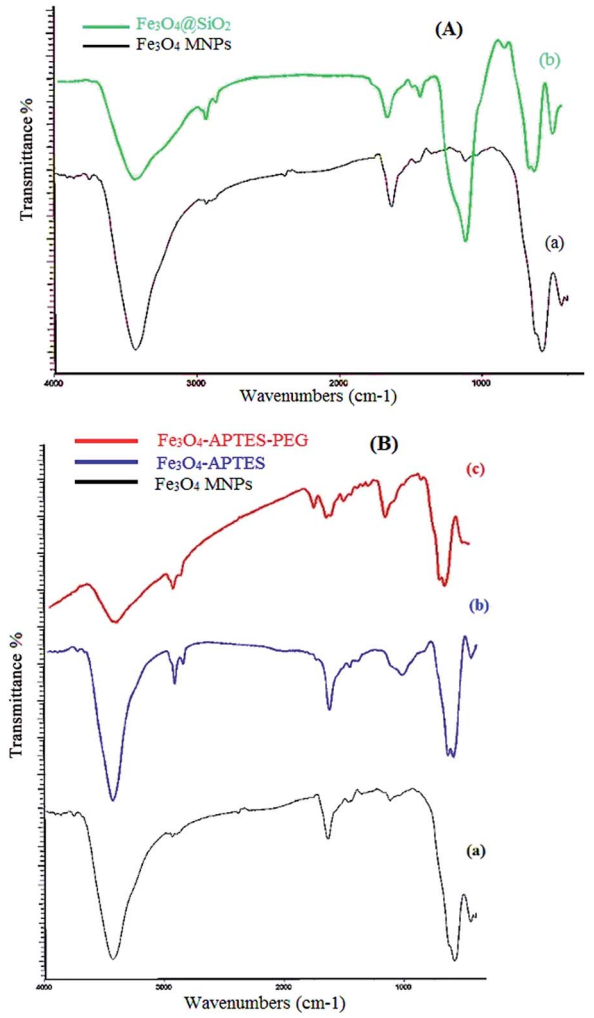

Fig. 3 The FTIR spectra in curve (A) for (a) Fe_3O_4 MNPs, (b) Fe_3O_4@SiO_2 MNPs and in curve (B) for (a) Fe_3O_4 MNPs, (b) Fe_3O_4-APTES MNPs, (c) Fe_3O_4-APTES–PEG.

(Fig. 3B, curve of (c)). The broad characteristic band around 3400 cm^{-1} is attributed to the hydroxyl groups at the end of PEG chains and the carboxyl groups. Overall, these results indicate the successive attachment of APTES and PEG on the surface of the magnetic NPs.

Vibrating sample magnetometer (VSM) analysis is used to evaluate magnetization of the pure and modified MNPs. Magnetization curves of prepared samples have been presented in Fig. 4. The saturation magnetization (M_s) value of MNPs, APTES-coated MNPs and Fe_3O_4@APTES–PEG were found to be 58.1, 50.35 and 48.33 electromagnetic units per gram (emu g^{-1}), respectively, while the values are 48.61 emu g^{-1} (Fe_3O_4@SiO_2) and 12 emu g^{-1} (Fe_3O_4@SiO_2@TiO_2) for the silica-coated particles. The reduction in saturation magnetization can be explained by the deposition of nonmagnetic shell layer coating on the magnetite cores and the lower content of Fe_3O_4 in the composite. From the Fig. 4, we can conclude that magnetic composite consists of APTES has better magnetic properties. However, the final M_s value of composites was sufficiently high, which could facilitate the separation and purification.

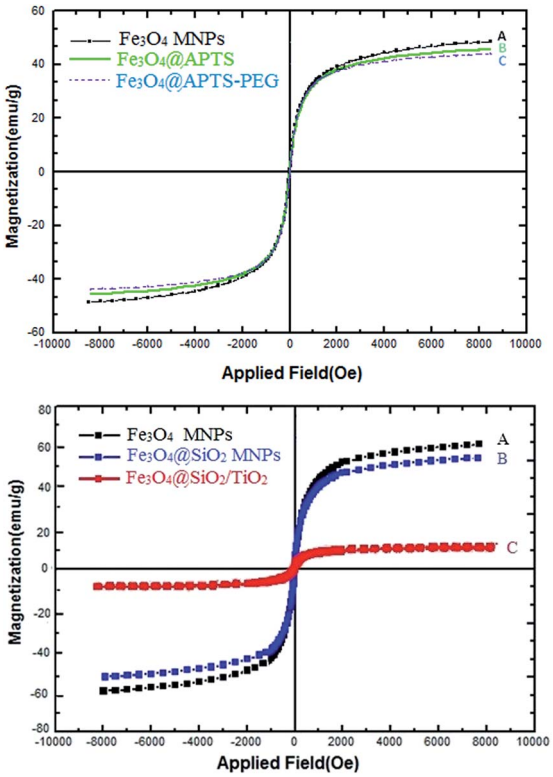

Fig. 4 VSM magnetization curves of Fe_3O_4 MNPs, Fe_3O_4@APTES, Fe_3O_4@APTES–PEG, Fe_3O_4@SiO_2 MNPs and Fe_3O_4@SiO_2/TiO_2.

The surface composition of Fe_3O_4-APTES–PEG@Ag and Fe_3O_4@SiO_2/TiO_2–Ag was confirmed by energy dispersive X-ray (EDX) spectroscopy as shown in Fig. 5A and B. In the EDS spectrum (inset of Fig. 5A) the detected elements are iron, silicon, nitrogen, carbon, cholor, silver and oxygen, confirming the expected composition of Fe_3O_4-APTES–PEG@Ag. The EDX spectrum of the Fe_3O_4@SiO_2/TiO_2–Ag (Fig. 5B) revealed the presence of iron, silicon, titanium, carbon, cholor, silver and oxygen signals.

Fig. 6 shows the UV-vis absorption spectra of Fe_3O_4-APTES–PEG@Ag prepared by $SnCl_2$ and $NaBH_4$, demonstrating the existence of Ag in the composites with the absorption peak at 400 nm. Also, atomic absorption spectroscopy (AAS) presented 38.9% and 31% Ag for Fe_3O_4-APTES–PEG@Ag (prepared by $NaBH_4$) and Fe_3O_4-APTES–PEG@Sn–Ag (prepared by $SnCl_2$), respectively.

The IR spectrum of PEG-Cl_4 (Fig. 7) was characterized by the following absorption bands: the –CH_2 stretching at 2870 cm^{-1}, C=N of cyanuric chloride fragments at 1716 and 1612 cm^{-1} and C–O stretching at 1107 and 1256 cm^{-1}. Moreover, in the ^1H NMR spectrum of PEG-Cl_4, the typical peak at 3.48–3.54 ppm correspond to terminated methylene groups (a) while the sharp peak at 3.63–3.68 ppm is attributed to methylene groups (b) in PEG structure.

2.2. Study on catalytic reduction

2.2.1. Study on the reduction kinetics of nitroaromatic compounds using Fe_3O_4@APTES–PEG–Ag nanocomposite. In order to evaluate the catalytic efficiency and reusability of

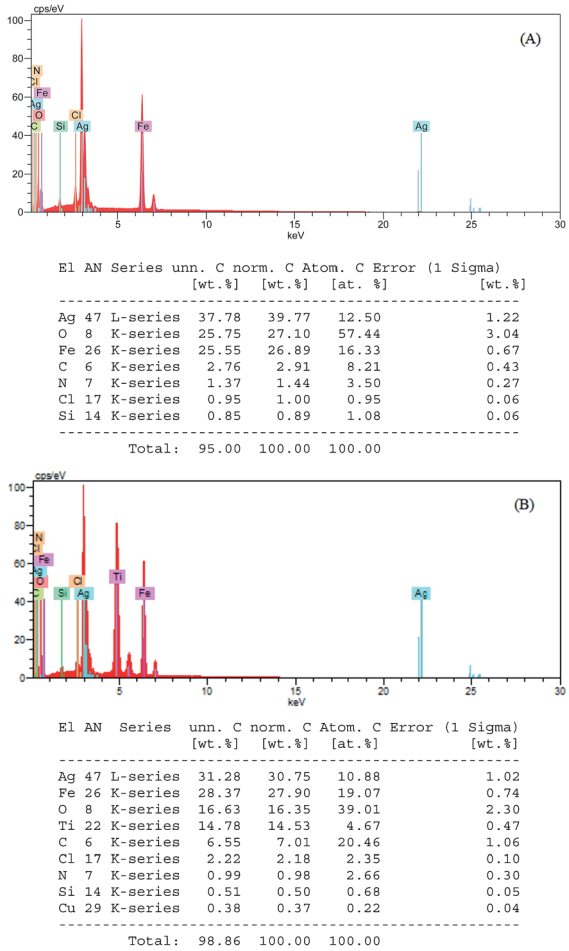

Fig. 5 EDS analyses of (A) Fe_3O_4-APTES–PEG@Ag (Ag: 39.77 wt%), (B) Fe_3O_4@SiO_2/TiO_2–Ag (Ag: 36.20 wt%).

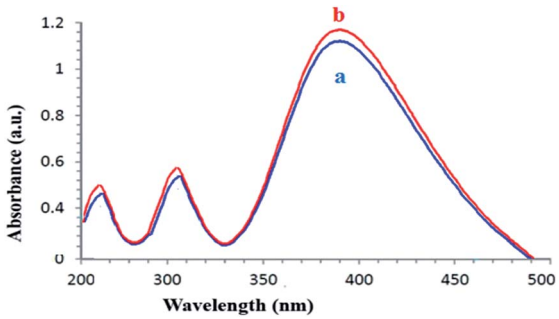

Fig. 6 UV-vis absorption spectra (a) Fe_3O_4-APTES–PEG@Sn–Ag and (b) Fe_3O_4-APTES–PEG@Ag.

Fe_3O_4@APTES–PEG–Ag, the catalytic reduction of 4-nitrophenol and 4-nitroaniline was performed in the presence of an excess $NaBH_4$ in aqueous medium. The reaction kinetics could be monitored using the time-dependent UV-vis absorption spectra. The original aqueous 4-NP solution exhibited the maximum absorption at 317 nm. As shown in Fig. 8A, upon the addition of freshly prepared $NaBH_4$ solution, the absorption maximum presented a red shift to 400 nm with change of the light yellow

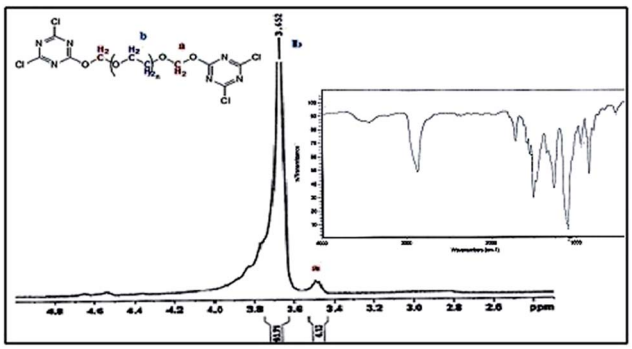

Fig. 7 FTIR and ^{1}H NMR spectra of PEG-Cl_4.

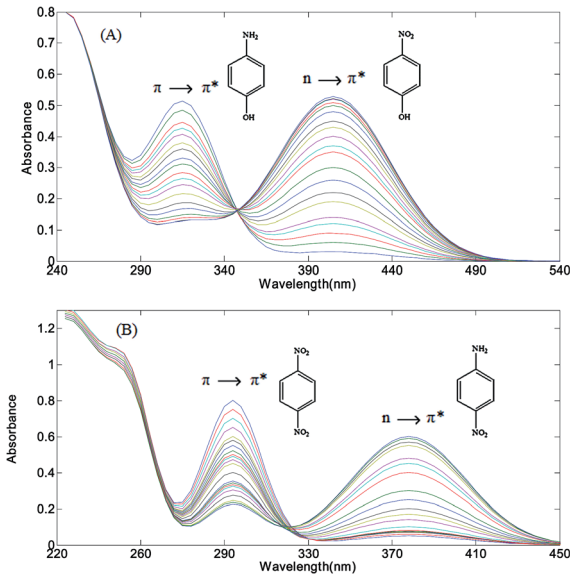

Fig. 8 UV-vis absorption spectra for the catalytic reduction of (A) 4-nitro phenol and (B) 4-nitro aniline by $NaBH_4$ over Fe_3O_4@APTES–PEG–Ag.

color to bright yellow, representative the formation of 4-nitorphenolate ions in alkaline condition. The absorption peak at 400 nm did not change with time which suggests the reduction does not take place in the absence of a catalyst. Upon the addition of catalyst, the intensity of the absorption peak at 400 nm gradually decreased with elapsed time. In the meantime, the appearance of a new absorption peak at 300 nm revealed the reduction of 4-NP to 4-AP. The reduction reaction could be completed with the disappearance of NO_2 peak at 400 nm and the increase in the absorbance at 300 nm evidenced by gradual fading of the yellow-green color of the reaction solution. Due to the presence of large excess $NaBH_4$ compared with 4-NP, it remained essentially constant during the reaction and the rate of reduction is independent of the borohydride content. This high concentration protects the 4-AP from aerial oxidation. Therefore, to evaluate the rate constants of the current catalytic reaction, the Langmuir–Hinshelwood apparent first-order kinetics model could be considered. In this mechanism, the reduction action takes place by the electron transfers from the

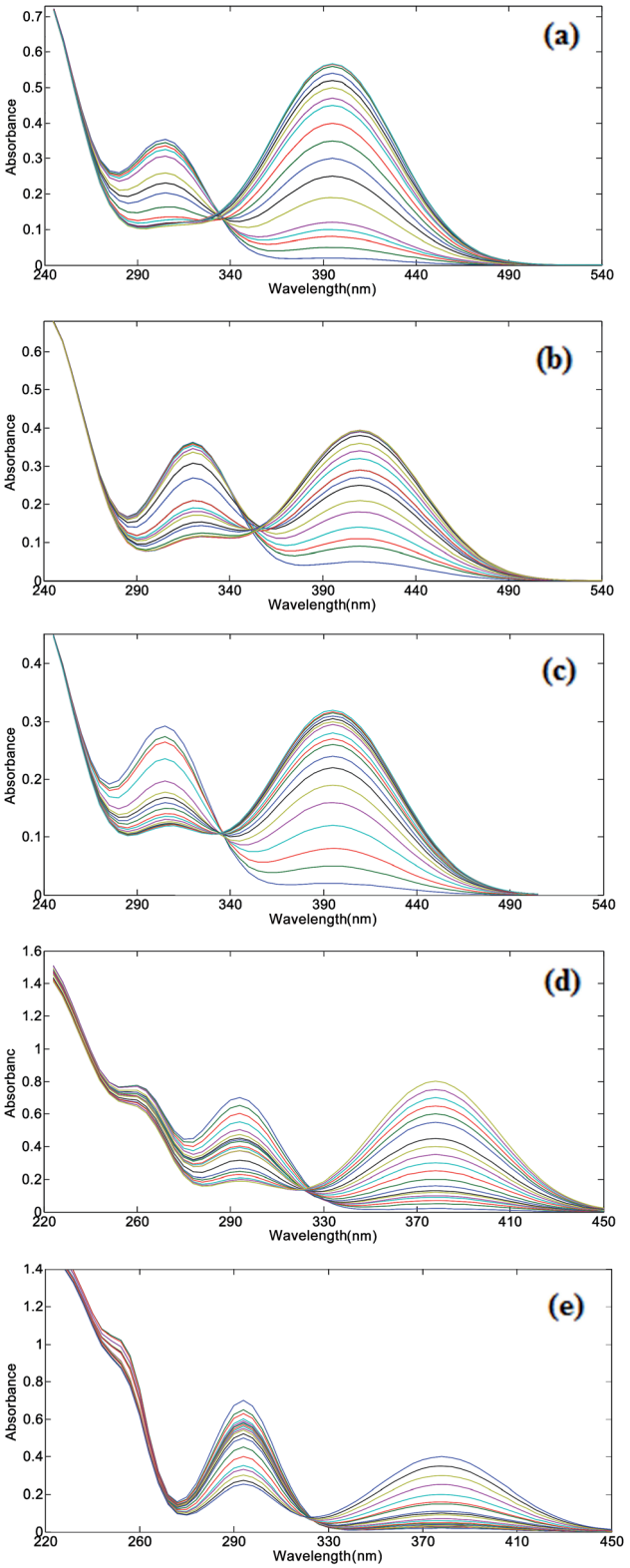

Fig. 9 UV-vis absorption spectra for the catalytic reduction of (a) 2-nitro phenol, (b) 3-nitro phenol, (c) 3-OMe-4-nitro phenol, (d) 2-nitro aniline, and (e) 3-nitro aniline using $NaBH_4$ over Fe_3O_4@APTES–PEG–Ag.

donor BH_4^- (hydrogen atom) to the acceptor 4-NP through the adsorption of both on the catalyst surface.

The same trend was also observed for the other nitrophenol and nitroaniline compounds (Fig. 9a–e).

The absorbance intensities of 4-NP are proportional to its concentration in the medium, the ratio of absorbance at time t to that at time 0 (A_t/A_0) is equivalent with the ratio of the concentration at time t to that at time 0 (C_t/C_0). Consequently, change of concentration of 4-NP with time t (C_t) can obtain from the decrease of the 400 nm peak intensity. Thus, the reaction kinetics equation can be described with equation of $dC_t/dt = -K_{app}t$ or $\ln(C_t/C_0) = \ln(A_t/A_0) = -K_{app}t$, where K_{app} is the apparent rate constant (min^{-1}) and t is the reaction time. Fig. 10a and b show the $\ln(C_t/C_0)$ *versus* reduction time (minutes) plots for the reduction of nitro compounds (NP and NA derivatives) using Fe_3O_4@APTES–PEG–Ag catalyst and the reduction of 4-NP in the presence of Fe_3O_4@APTES–PEG–M (M = Cu, Ag, Co and Ni) catalysts, respectively. As shown in Fig. 10a and b, good linear relationship between $\ln(C_t/C_0)$ and reaction time t was observed which suggests the reaction follows first-order kinetics.

2.2.2. Temperature dependence and calculation of activation energy. The kinetic reaction rate constants (K_{app}) and correlation coefficients (R^2) in the presence of the catalyst are estimated from the slopes of the linearly fitted plots and were summarized in Tables 1 and 2. The activation energy was calculated from the set of kinetic data using the Arrhenius equation: $\ln K_{app} = \ln A - (E_a/RT)$, where E_a is activation energy, A is the Arrhenius factor, K_{app} is the rate constant at temperature T (in Kelvin) and R is the ideal gas constant. A larger activation energy value shows higher sensitivity of the kinetic constant K_{app} to reaction temperature. The values of activation energy are also found in Tables 1 and 2.

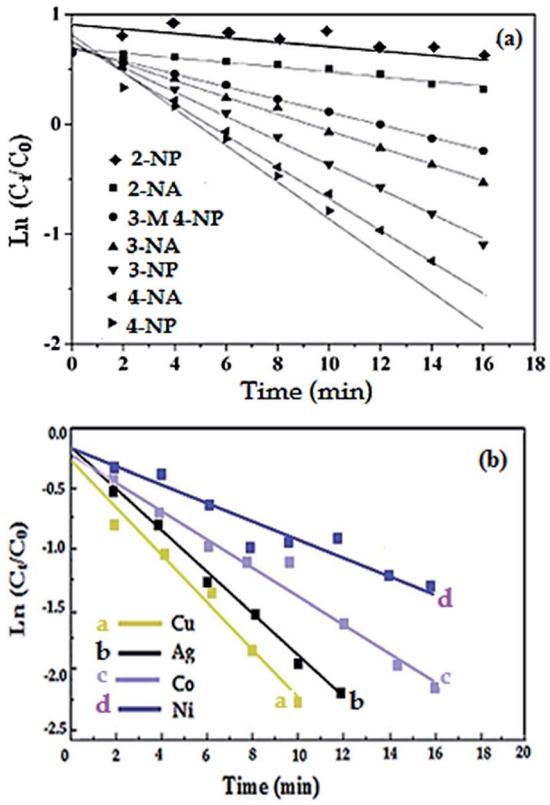

Fig. 10 $\ln(C_t/C_0)$ *versus* reaction time (minutes) plots for the reduction of (a) nitroaromatics using $NaBH_4$ in the presence of Fe_3O_4@APTES–PEG–Ag and (b) *p*-nitrophenol using $NaBH_4$ in the presence of Fe_3O_4@APTES–PEG–M.

2.2.3. Reduction of other nitro-compounds. Kinetic reduction of two kind different nitro-compounds, *e.g.*, NP and NA, was also studied using $NaBH_4$ in the presence of Fe_3O_4@APTES–PEG–Ag catalyst. A comparative study shows that the rate constants of reduction and the activation energy follows the sequence of 4-NP > 4-NA > 3-NP > 3-NA > 3-m 4-NP > 2-NA > 2-NP. In general, the activation energy of the reduction of *para*-substituted nitro compounds is lower than that of *ortho*-substituted nitro compounds. This can be explained owing to the steric effect of the *ortho*-substituted nitro compounds. These results indicate the efficiency and the generality of this catalyst toward the reduction of different nitrophenols and nitroanilines. As shown in Table 1, the as-prepared catalyst exhibited high catalytic efficiency with excellent yields in the reduction of a series of nitro-aromatic compounds regardless of the types and position of the substituents.

To confirm the difference in catalytic efficiency of catalysts with different metals, we have compared their reduction rate constants for 4-NP. The first-order rate constants (K_{app}), activation energy and correlation coefficients for the catalytic reduction reactions of 4-NP using Fe_3O_4@APTES–PEG–M (M = Cu, Ag, Co, Ni, Pb, Zn and Mn) have been presented in Table 2. Among mentioned metals in theses catalysts, Pb, Zn and Mn metals were inactive and reaction was unchanged over times, which suggests the reduction did not proceed in the presence of these catalysts. The present study presents that the Fe_3O_4@APTES–PEG–M nanocomposites (M = Cu, Ag, Co, Ni) are very effective with excellent performance for the catalytic reduction of 4-nitrophenol. A comparative study revealed that the order of rate constants from highest to lowest is Cu > Ag > Ni > Co. The corresponding first order rate constants are 1.051, 0.8871, 0.9743 and 0.9788 min^{-1} for catalysts containing Cu, Ag, Co and Ni, respectively. These results clearly demonstrate the high catalytic activity of the Fe_3O_4@APTES–PEG–Cu nanocomposites over others systems. Despite the high performance copper nanocatalyst in the reduction process, instability and oxidation is one of its major disadvantages. Therefore, Fe_3O_4@APTES–PEG–Ag is better option than others in the reduction process owing to the benefit of high performance and optimal stability.

In order to compare the catalytic activity of Fe_3O_4@APTES@PEG–Ag catalyst with the ones reported in the literature containing Ag NPs, it is not exclusively appropriate to compare the rate constant. Hence, the activity parameter $\kappa = K/m$ (the ratio of rate constant K over the total weight of the catalyst m) is employed to indicate its high catalytic performance comparable to some research results (Table 3).

2.2.4. Influence of catalytic dosage of Fe_3O_4@APTES–PEG–Ag on reduction of 4-NP. Furthermore, the influence of different amounts of Fe_3O_4@APTES–PEG–Ag catalyst was

Table 1 Kinetic and thermodynamic parameters for the catalytic reduction of the nitroaromatic compounds by $NaBH_4$ over Fe_3O_4@APTES–PEG–Ag

Entry	Compound	Product	R^2	K_{app} (min^{-1})	E_a (kJ min^{-1})	Time (min)	Yield (%)
1	2-NO_2 phenol	**3a**	0.9812	0.6712	36.13	20	94
2	3-NO_2 phenol	**3b**	0.9742	0.7643	32.01	14	97
3	4-NO_2 phenol	**3c**	0.9983	0.8871	22.84	10	99
4	3-OMe-4-NO_2 phenol	**3d**	0.9617	0.6816	33.41	16	97
5	2-NO_2 aniline	**3e**	0.9853	0.6726	35.98	21	94
6	3-NO_2 aniline	**3f**	0.9781	0.7619	32.78	16	88
7	4-NO_2 aniline	**3g**	0.9901	0.8863	23.20	12	99

Table 2 Kinetic and thermodynamic parameters for the catalytic reduction of the *p*-nitrophenol by $NaBH_4$ over Fe_3O_4@APTES–PEG–M

Entry	Compound	Metal	Product	R^2	K_{app} (min^{-1})	E_a (kJ min^{-1})	Time (min)	Yield (%)
1	4-NO_2 phenol	Cu	**3c**	0.9873	1.051	19.41	10	99
2	4-NO_2 phenol	Co	**3c**	0.9782	0.9743	23.51	14	98
3	4-NO_2 phenol	Ni	**3c**	0.9788	0.9788	23.94	14	98
4	4-NO_2 phenol	Ag	**3c**	0.8871	0.8871	22.84	10	98

Table 3 The comparison of catalytic activity between some reported catalysis and Fe_3O_4@APTES@PEG–Ag

Entry	Nanocatalyst	Catalyst (mg)	K (s^{-1})	κ (s^{-1} g^{-1})	Ref.
1	Ag NP/C	1	1.69×10^{-3}	1.69	51
2	Fe_3O_4@SiO_2–Ag	1	7.67×10^{-3}	7.67	52
3	Fe_3O_4/SiO_2–Ag	0.02	5.50×10^{-3}	275	53
4	Fe_3O_4@C@Ag	0.01	3.72×10^{-3}	372	54
5	Ag NP-PG-5K	0.004	5.50×10^{-3}	1375	55
6	Fe_3O_4@APTES@PEG–Ag	0.01	14.8×10^{-3}	1480	This work

studied as well on reduction of 4-NP. As expected with the increasing amount of catalyst, the rate constant increased, which is due to the concentration of the catalytically active site. Rate constant values are plotted against varying concentrations of catalyst as shown in Fig. 11. It was found that the first-order rate constant increased linearly with the catalyst amount.

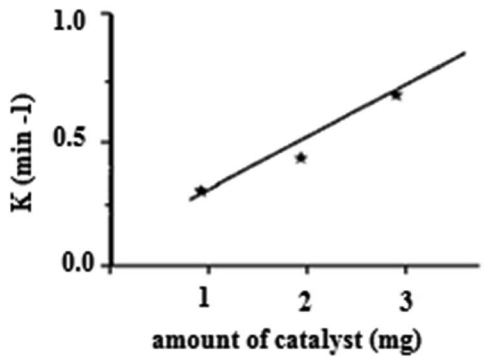

Fig. 11 The effect of the dosage of catalyst on the catalytic reduction of the *p*-nitrophenol.

2.2.5. Catalytic recyclability of Fe_3O_4@APTES–PEG–Ag. Moreover, the possibility of recoverability and reusability of Fe_3O_4@APTES–PEG–Ag catalyst were investigated. The obtained nanocatalysts exhibited excellent magnetic separability and good reusability upon five successive cycles of reduction. The rate constant for the conversion against the number of cycles is plotted in Fig. 12. As shown in Fig. 12 with the increase of cycle, the corresponding rate constant was only

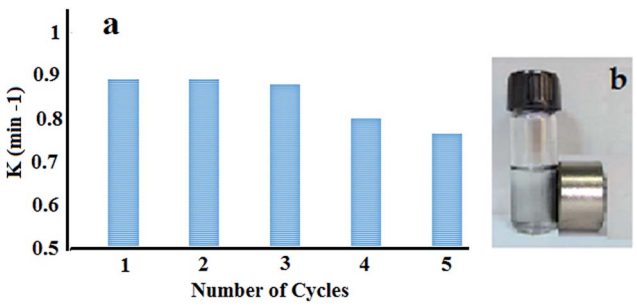

Fig. 12 (a) K_{app} in different cycles of catalytic reduction of *p*-nitrophenol in the presence of $NaBH_4$ with Fe_3O_4@APTES–PEG–Ag as catalyst, (b) magnetic separation of catalyst.

slightly decreased as compared with fresh catalyst indicative of stable and excellent recycling efficiency of the catalyst.

3. Experimental

3.1. Characterization

Fourier transform infrared (FTIR) spectra were determined on a Nicolet Magna-IR 550 spectrophotometer using a liquid sample or KBr powder-pressed pellets in the range of 400–4000 cm^{-1}. Transmission electron microscopy (TEM) analysis was performed on a LEO 912-AB resolution electron microscope. Scanning electron microscopy (SEM) experiments were recorded on a Hitachi 4160 FESEM microscope equipped with EDS operated at a 20 kV accelerating voltage. X-ray diffraction (XRD) patterns were performed on a Holland Philips Xpert X-ray diffractometer, using Cu K (1.54 Å) radiation at 40 kV, the scan range (2θ) was from 10° to 100°. ^{1}H nuclear magnetic resonance (^{1}H NMR) spectra were recorded on a Bruker DRX-400 spectrometer with $DCCl_3$ as solvent and TMS as interior standard. Thermogravimetric analysis (TGA) was carried out on a TGA ARES Rheometric Scientific thermogravimetric analyzer with a heating rate of 10 °C min^{-1} under an argon atmosphere. Magnetic measurements were measured using a BHV-55 VSM (Vibrating Sample Magnetometer) system at room temperature. UV spectroscopy measurements were performed on a UV GBC Centra 6 UV-visible spectrophotometer. Atomic absorption spectroscopy (AAS) analysis was obtained using Analytical Jena Contra 700 spectrometer (Germany). Sonication was performed in VGA 3025 K Ultrasonic dental scaler with a frequency of 30 kHz and a nominal power of 100 W.

3.2. Preparation and surface modification of the magnetic Fe_3O_4 NPs

3.2.1. General procedure for the preparation of Fe_3O_4@APTES@PEG–Ag MNPs. The magnetic Fe_3O_4 NPs were synthesized through the chemical co-precipitation of Fe^{3+} and Fe^{2+} ions with a molar ratio of 2 : 1 in alkaline medium.[56] Typically, under vigorous mechanical stirring, 100 mL freshly prepared aqueous mixture of ferric chloride ($FeCl_3 \cdot 6H_2O$, 5.83 g) and ferrous chloride ($FeCl_2 \cdot 4H_2O$, 2.15 g) was added into ammonia solution (30 mL) under argon protection at 60 °C (500 rpm). The color of the suspension turned black immediately and the reaction continued for another 30 min. After magnetically separation and washing with deionized water several times, the obtained Fe_3O_4 MNPs were dried under vacuum at 60 °C for 24 h. To produce silanized Fe_3O_4 NPs (Fe_3O_4@APTES), chemical coating of Fe_3O_4 NPs with a common amino-silane coupling agent, 3-aminopropyltriethoxysilane (APTES) was performed as described previously.[57] Briefly, the obtained MNPs powder (2 g) was dispersed in 250 mL ethanol/water (volume ratio, 1 : 1) solution by sonication for 30 min. Then, in order to impart the amino functional group, 2.5 mL of APTES was added to the mixture and the reaction continued under reflux and argon gas flow for 12 h. Lastly, the resulting black precipitate was separated by magnetic decantation, washed five times with ethanol and dried in a vacuum oven at 80 °C. Subsequently, APTES-modified magnetite nanoparticles were coated with polyethylene glycol (PEG) to achieve MNPs@organosilane@polymer core–shell–shell nanostructures (MNPs@APTES–PEG). PEG (M_n = 1000) was functionalized by cyanuric chloride according to reported procedure in the literature.[58] In short, a solution of 5 g poly(ethylene glycol) and 0.4 g sodium hydroxide in 10 mL of water was dropped to a solution of 10 g cyanuric chloride in 200 mL dichloromethane at 0 °C. The mixture was stirred for 1 h at room temperature and then was refluxed for 6 h. The obtained functionalized PEG (PEG-Cl_4) was filtered and precipitated in diethyl ether as a white solid. 0.6 g of PEG-Cl_4 was then dissolved in 50 mL of dried THF and 0.3 g of Fe_3O_4@APTES MNPs was added to this solution. Then, the mixture was dispersed under sonication for 10 min. Finally, the product was separated using a magnet and washed several times with absolute ethanol and dried at 60 °C under vacuum for 24 h. Then, was directly used for coating with silver nanoparticles. Typically, 0.12 g of APTES–PEG modified Fe_3O_4 NPs and 0.3 g of $AgNO_3$ were dispersed into 20 mL and 50 mL ethanol under ultrasonication, respectively. Then, the resultant solutions were mixed together and maintained at 50 °C under the mechanical stirring condition. After 1 h, a fresh prepared aqueous solution of 1 mL $NaBH_4$ (0.01 g L^{-1}) was added using a syringe. Ultimately, a black precipitate of Ag NPs was formed onto the magnetic nanocomposites by reducing of $AgNO_3$ with $NaBH_4$. The reaction was continued for other 3 h and the final product was collected by magnetic separation, washed with ethanol for three times and dried at room temperature under vacuum for 24 h. At last, the other metals were decorated on Fe_3O_4@APTES–PEG using precursors of $CuSO_4 \cdot 5H_2O$, $Co(CH_3CO_2)_2 \cdot 2H_2O$, $NiCl_2 \cdot 2H_2O$, $ZnCl_2$, $MnSO_4 \cdot 5H_2O$ and $Pb(CH_3CO_2)_2 \cdot 2H_2O$ according to above-mentioned method except that the reaction was carried out in argon atmosphere to prevent the formation of transition metal oxides. The other method for preparation of Ag modified Fe_3O_4@APTES–PEG nanocomposites was carried out following the bellow experimental procedure. As-prepared magnetite@APTES–PEG (100 mg in 40 mL distilled water) and $SnCl_2 \cdot 2H_2O$ (0.5 g in 100 mL of 0.02 M HCl) were dispersed under ultrasonic treatment, separately. The dispersions were mixed and stirred under mechanical agitation for 1 h. Afterward, 75 mL of the ammonia solution of silver [$Ag(NH_3)^{2+}$] (0.11 M) was dropped into above mixture and sonicated for additional 1 h. The product was separated using an external magnet and washed using water and ethanol three times and dried at 50 °C for 12 h. Based on the above descriptions, the coating approaches are schematically illustrated in Scheme 2.

3.2.2. General procedure for the preparation of Fe_3O_4@SiO_2/TiO_2–Ag MNPs. After preparing the magnetic Fe_3O_4 NPs through the chemical co-precipitation, the silica coating was performed through a Stöber sol–gel process[31] *via* hydrolysis of tetraethyl orthosilicate (TEOS) as silica source in basic solution of ammonia, ethanol and deionized water. In a typical procedure, 1 g of as-prepared Fe_3O_4 nanoparticles was homogeneously dispersed in the mixture of 80 mL of absolute ethanol, 16 mL of deionized water by sonication for 30 min. After adding

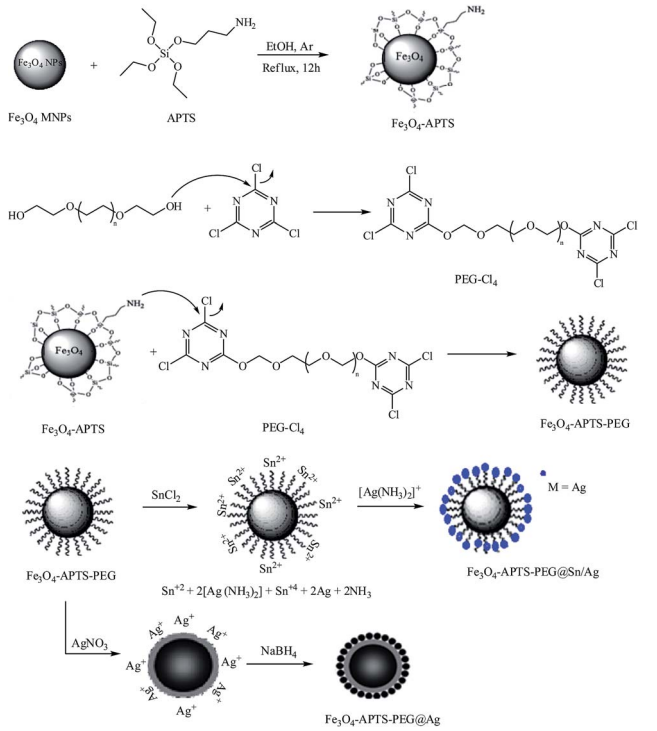

Scheme 2 Schematic illustration of the procedure for the preparation of the Fe_3O_4@APTES/PEG–Ag.

2 mL of aqueous ammonia (NH_4OH, 25 wt%), 2 mL TEOS was added to the reaction solution under mechanical stirring (500 rpm). The resulting solution was further mechanically stirred for 24 h at room temperature to obtain magnetic nanoparticles coated by silica. The Fe_3O_4/SiO_2 NPs were magnetically collected, washed with water and ethanol and then dried at 90 °C for 24 h. The second coating with titanium dioxide was performed through a sol–gel method. Briefly, 0.5 g Fe_3O_4/SiO_2 particles were dispersed into a solution of 2.5 mL tetraethyl orthotitanate (TEOT) and 22 mL absolute ethanol under mechanical stirring for 30 min at 40 °C. After that, the mixture containing 1.5 mL of water, 0.2 mL hydrochloric acid and 22 mL absolute ethanol was added in drops to the suspension. Subsequently, the suspension was stirred continuously for 2 h until gel was formed. The resulting nanocomposite was magnetically separated, washed with ethanol several times and dried at 80 °C under vacuum. Subsequently, calcination was carried out at 450 °C in air for 1 h to convert the TiO_2 outer shell from amorphous phase to photocatalytically active crystalline anatase phase. To locate Ag NPs on the surface of Fe_3O_4@SiO_2/TiO_2, photoreducing Ag(I)–EDTA to Ag metal on the titania surface was performed. Typically, 100 mg Fe_3O_4@SiO_2/TiO_2 was added into 100 mL deionized water and irradiated by UV-light for 30 min to remove any impurities. Afterwards, equimolar amounts of silver nitrate ($AgNO_3$, 1.0 wt% Ag(I)) and ethylenediaminetetraacetic acid (EDTA) were dissolved in deionized water. Subsequently, 10 mL of Ag(I)–EDTA aqueous solution was added into the above suspension. The suspension was stirred with vigorous mechanical stirring and irradiated by UV-light for

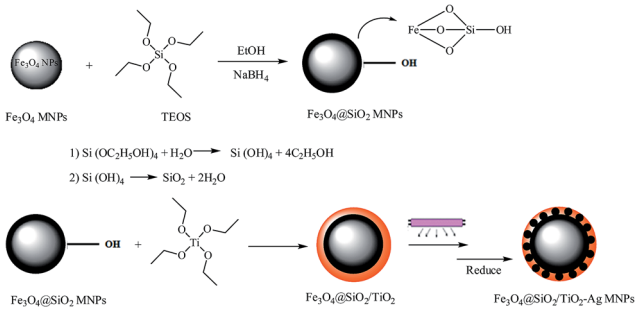

Scheme 3 Schematic representative for preparation of the Fe_3O_4@-SiO_2/TiO_2–Ag MNPs.

2 h under argon atmosphere. At last, the precipitate was collected by magnetic separation, washed with distilled water, and then dried at 70 °C for 24 h. To better understand of the coating process, the overall synthetic procedure has been illustrated in Scheme 3.

3.3. Catalytic reduction of nitroaromatic compounds

3.3.1. General procedure for the catalytic reduction of 4-nitrophenol by Fe_3O_4@APTES/PEG–Ag MNPs in the presence of $NaBH_4$. The catalytic redox reaction of 4-NP was performed in a standard quartz cell and monitored using UV-vis spectroscopy at room temperature. In general, 0.9 mL of a freshly prepared $NaBH_4$ aqueous solution (0.2 M) was added to a quartz cell containing 0.1 mL of aqueous 4-NP solution (0.005 M) and 2.0 mL of distilled water. Immediately, the nitrophenol was converted into nitrophenolate anion and the solution color turned from light yellow to yellow-green rapidly. Subsequently, catalyst (0.01 mg) was added to the mixture. Immediately after the addition of catalyst, the absorption spectra were continually recorded by UV-vis spectrophotometer over a scanning range of 200–700 nm with a time interval of 2 min to record the change in absorbance. The initially obtained data can be designed as the start time of reaction, $t = 0$. The rate constant of the redox reaction was determined by determining the change in absorption at 400 nm as a function time. In fact, the bright yellow solution gradually changed to transparent as the reaction proceeded, indicating the decrease in absorbance and the reduction of 4-NP as shown in Scheme 4.

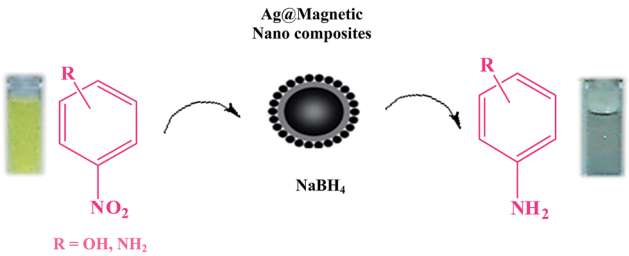

Scheme 4 Illustration of the reduction process of nitroaromatic compounds by $NaBH_4$ in the presence of Fe_3O_4@APTES/PEG–Ag MNPs.

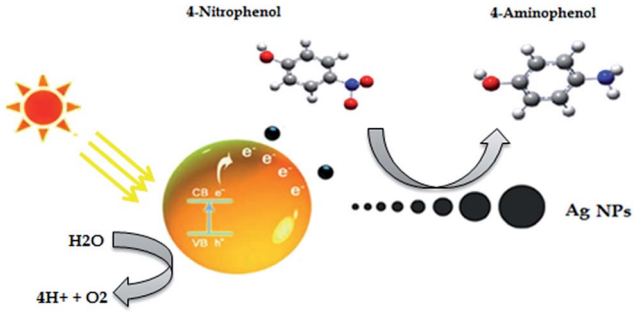

Scheme 5 Illustration of the reduction route of *p*-nitrophenol using Fe_3O_4@SiO_2/TiO_2–Ag under UV-light.

3.3.2. General procedure for the catalytic reduction of 4-nitrophenol by Fe_3O_4@SiO_2/TiO_2–Ag MNPs in the presence of $NaBH_4$. In a typical reaction, 50 mL of 4-nitrophenol (0.0005 M) was mixed with 3 mg of Fe_3O_4@SiO_2/TiO_2–Ag photocatalyst. The suspension was mechanically stirred and irradiated by UV-light for 5 h. Electron transfer was shown in bellow reduction equation. The yellow color of solution gradually vanished, which it indicated that the reaction was finished. The product was then precipitated from solution by magnetic force, washed, and dried. The reduction procedure was illustrated in Scheme 5.

$$e_{CB}^- + h_{VB}^+ \rightarrow TiO_2 + h\nu \quad (1)$$

$$Ag^+ + e_{CB}^- \rightarrow Ag^0 \quad (2)$$

$$2H_2O + 4h_{VB}^+ \rightarrow 4H^+ + O_2 \quad (3)$$

$$Ag^0 + Ag^+ + e_{CB}^- \rightarrow Ag_2 \rightarrow Ag_n \quad (4)$$

4. Conclusions

In this study, magnetically separable nanostructures with excellent catalytic properties were developed for the reduction of nitroaromatics using $NaBH_4$ as the reducing agent. The as-prepared nanocomposites are composed of a central magnetite core, an interlayer of silica or ATPES, a shell of titania or PEG, and highly dispersed Ag nanoparticles. These nanocomposites show high activity, good selectivity and excellent recyclability in the catalytic reduction of nitroaromatic compounds. The synthesized multilayer-structured composites were characterized using scanning electron microscope (SEM), energy dispersive X-ray (EDX), X-ray powder diffraction (XRD), Fourier transform infrared spectroscopy (FT-IR), vibrating sample magnetometer (VSM) and Thermal Gravimetric Analysis (TGA). This work also provides a cost effective, green and mild route to prepare composite structures combined with magnetic cores with high stability. Furthermore, the fast magnetic separation and stability of the catalysts over several separation cycles are advantageous in environmental, commercial and biotechnological practical applications. The rate constants are in harmony with first-order kinetic model and have been improved with the increases in temperature and amount of catalyst.

Acknowledgements

This work was financially supported by University of Kashan Research Council (Grant No. 363022/24).

Notes and references

1 K. L. Thomas-Keprta, D. A. Bazylinski, J. L. Kirschvink, S. J. Clemett, D. S. McKay, S. J. Wentworth, H. Vali, E. K. Gibson and C. S. Romanek, *Geochim. Cosmochim. Acta*, 2000, **64**, 4049.
2 J. Qiu, M. Xiong, R. Liang, H. Peng and F. Liu, *Biosens. Bioelectron.*, 2009, **24**, 2649.
3 S. Wang, Y. Tan, D. Zhao and G. Liu, *Biosens. Bioelectron.*, 2008, **23**, 1781.
4 S. Sun, C. B. Murray, D. Weller, L. Folks and A. Moser, *Science*, 2000, **287**, 1989.
5 V. Skumryev, S. Stoyanov, Y. Zhang, G. Hadjipanayis, D. Givord and J. Nogues, *Nature*, 2003, **423**, 850.
6 C. Lu, Y. Hung, J. Hsiao, M. Yao, T. Chung, Y. Lin, S. Wu, S. Hsu, H. Liu, C. Mou, C. Yang, D. Huang and Y. Chen, *Nano Lett.*, 2007, **7**, 149.
7 Y. Weizmann, F. Patolsky, E. Katz and I. Willner, *J. Am. Chem. Soc.*, 2003, **125**, 3452.
8 J. L. Gong, Y. Liang, Y. Huang, J. W. Chem, J. H. Jiang, G. L. Shen and R. Q. Yu, *Biosens. Bioelectron.*, 2007, **22**, 1501.
9 S. Kayal and R. V. Ramanujan, *Mater. Sci. Eng., C*, 2010, **30**, 484.
10 L. Zhang, Y. Zhai, N. Gao, D. Wen and S. Dong, *Electrochem. Commun.*, 2008, **10**, 1524.
11 Y. H. Deng, C. H. Deng, D. W. Qi, C. Liu, J. Liu, X. M. Zhang and D. Y. Zhao, *Adv. Mater.*, 2009, **21**, 1377.
12 D. S. Jiang, S. Y. Long, J. Huang, H. Y. Xiao and J. Y. Zhou, *Biochem. Eng. J.*, 2005, **25**, 15.
13 Y. R. Chemla, H. L. Grossman, Y. Poon, R. Mc Dermott, R. Stevens, M. D. Alper and J. Clarke, *Proc. Natl. Acad. Sci. U. S. A.*, 2000, **97**(26), 14268.
14 J. Klostergaard and C. E. Seeney, *Maturitas*, 2012, **73**, 33.
15 S. C. Mc Bain, H. H. Yiu and J. Dobson, *Int. J. Nanomed.*, 2008, **3**(2), 169.
16 J. W. Bulte and D. L. Kraitchman, *NMR Biomed.*, 2004, **17**(7), 484.
17 L. Josephson, *BioMEMS Biomed. Nanotechnol.*, 2006, 227.
18 C. L. Dennis, A. J. Jackson, J. A. Borchers, R. Ivkov, A. R. Foreman and P. J. Hoopes, *J. Phys. D: Appl. Phys.*, 2008, **41**(13), 134020.
19 L. Y. Zhang, H. C. Gu and X. M. Wang, *J. Magn. Magn. Mater.*, 2007, **311**, 228.
20 J. Li, Y. Zhou, M. Li, N. Xia, Q. Y. Huang, H. Do, Y. N. Liu and F. M. Zhou, *J. Nanosci. Nanotechnol.*, 2011, **11**, 10187.
21 H. Y. Park, M. J. Schadt, L. Y. Wang, I. I. S. Lim, P. N. Njoki, S. H. Kim, M. Y. Jang, J. Luo and C. J. Zhong, *Langmuir*, 2007, **23**, 9050.
22 G. Zhao, J. J. Feng, Q. L. Zhang, S. P. Li and H. Y. Chen, *Chem. Mater.*, 2005, **17**(12), 3154.
23 D. L. Leslie-Pelecky, V. Labhasetwar and J. R. H. Kraus, in *Advanced Magnetic Nanostructures*, ed. D. Sellmyer and R. Skomski, Springer, US, 2006.

24 (*a*) X. Wang, C. Zhang, X. Wang and H. Gu, *Appl. Surf. Sci.*, 2007, **253**(18), 7516; (*b*) Y. Arum, H. W. Kang and J. H. Oh, *Fish. Aquat. Sci.*, 2015, **18**(1), 89.
25 (*a*) M. E. Khosroshahi and L. Ghazanfari, *Mater. Sci. Eng., C*, 2012, **32**(5), 1043; (*b*) S. C. Pang, W. H. Khoh and S. F. Chin, *J. Mater. Sci. Technol.*, 2011, **27**(10), 873; (*c*) J. Q. Ma, S. B. Guo, X. H. Guo and H. G. Ge, *J. Nanopart. Res.*, 2015, **17**(7), 1.
26 P. P. Yang, Z. W. Quan, Z. Y. Hou, C. X. Li, X. J. Kang, Z. Y. Cheng and J. Lin, *Biomaterials*, 2009, **30**, 4786.
27 Z. Zhang, L. Zhang, L. Chen, L. G. Chen and Q. Wan, *Biotechnol. Prog.*, 2006, **22**, 514.
28 Y. Sun, L. Duan, Z. Guo, Y. Duan Mu, M. Ma, L. Xu, Y. Zhang and N. Gu, *J. Magn. Magn. Mater.*, 2005, **285**(1–2), 65.
29 Y. H. Deng, C. C. Wang, J. H. Hu, W. L. Yang and S. K. Fu, *Colloids Surf., A*, 2005, **262**, 87.
30 Y. A. Barnakov, M. H. Yu and Z. Rosenzweig, *Langmuir*, 2005, **21**, 7524.
31 W. Stöber, A. Fink and E. Bohn, *J. Colloid Interface Sci.*, 1968, **26**(1), 62.
32 S. Santra, R. Tapec, N. Theodoropoulou, J. Dobson, A. Hebard and W. H. Tan, *Langmuir*, 2001, **17**, 2900.
33 H. Liu, Z. Jia, S. Ji, Y. Zheng, M. Li and H. Yang, *Catal. Today*, 2011, **175**(1), 293.
34 T. Kojima, T. A. Gad-Allah, S. Kato and S. Satokawa, *J. Chem. Eng. Jpn.*, 2011, **44**(9), 662.
35 X. Song and L. Gao, *J. Am. Ceram. Soc.*, 2007, **90**, 4015.
36 T. A. Gad-Allah, S. Kato, S. Satokawa and T. Kojima, *Solid State Sci.*, 2007, **9**(8), 737.
37 D. H. Zhang, G. D. Li, J. X. Li and J. S. Chen, *Chem. Commun.*, 2008, (29), 3414.
38 L. Ai, C. Zeng and Q. Wang, *Catal. Commun.*, 2011, **14**(1), 68.
39 L. Li, E. S. G. Choo, X. Tang, J. Ding and J. Xue, *Acta Mater.*, 2010, **58**, 3825.
40 (*a*) M. M. A. Nikje, S. T. Moghaddam, M. Noruzian, M. A. F. Nejad, K. Shabani, M. Haghshenas and S. Shakhesi, *Colloid Polym. Sci.*, 2014, **292**(3), 627; (*b*) H. Yin, Y. Zhou, T. Liu, T. Tang, S. Ai and L. Zhu, *J. Solid State Electrochem.*, 2012, **16**(2), 731.
41 H. Cao, J. He, L. Deng and X. Gao, *Appl. Surf. Sci.*, 2009, **255**(18), 7974.
42 K. Can, M. Ozmen and M. Ersoz, *Colloids Surf., B*, 2009, **71**, 154.
43 B. Feng, R. Y. Hong, L. S. Wang, L. Guo, H. Z. Li, J. Ding, Y. Zheng and D. G. Wei, *Colloids Surf., A*, 2008, **328**(1), 52.
44 K. Mullick, M. J. Witcomb and M. S. Scurrell, *J. Mater. Sci.*, 2004, **39**, 4459.
45 T. Vincent and E. Guibal, *Langmuir*, 2003, **19**, 8475.
46 M. Ahmaruzzaman and S. L. Gayatri, *J. Chem. Eng. Data*, 2010, **55**, 4614.
47 K. L. Wu, X. W. Wei, X. M. Zhou, D. H. Wu, X. W. Liu, Y. Ye and Q. Wang, *J. Phys. Chem. C*, 2011, **115**, 16268.
48 T. Swathi and G. Buvaneswari, *Mater. Lett.*, 2008, **62**, 3900.
49 J. R. Chiou, B. H. Lai, K. C. Hsu and D. H. Chen, *J. Hazard. Mater.*, 2013, **248**, 394.
50 M. Tumma and R. Srivastava, *Catal. Commun.*, 2013, **37**, 64.
51 S. Tang, S. Vongehr and X. Meng, *J. Phys. Chem. C*, 2010, **114**, 977.
52 Y. Chi, Q. Yuan, Y. Li, J. Tu, L. Zhao, N. Li and X. Li, *J. Colloid Interface Sci.*, 2012, **383**, 96.
53 K. S. Shin, Y. K. Cho, J. Y. Choi and K. Kim, *Appl. Catal., A*, 2012, **413–414**, 170.
54 Q. An, M. Yu, Y. Zhang, W. Ma, J. Guo and C. Wang, *J. Phys. Chem. C*, 2012, **116**, 22432.
55 B. Baruah, G. J. Gabriel, M. J. Akbashev and M. E. Booher, *Langmuir*, 2013, **210**(21), 12341.
56 T. T. Dung, T. M. Danh, N. H. Duc and D. M. Chien, *J. Phys.: Conf. Ser.*, 2009, **187**(1), 012048.
57 P. Lu, J. L. Zhang, Y. L. Liu, D. H. Sun, G. X. Liu, G. Y. Hong and G. Z. Ni, *Talanta*, 2010, **82**, 450.
58 H. Namazi and M. Adeli, *Polymer*, 2005, **46**, 10788.